

The Instability of Painlevé Equations in Recovering Largest Eigenvalue Distributions of GUE, LUE, JUE and an Attempt of Solution to It

Haonan Gu

November 2025

Abstract

The distribution of the largest eigenvalue for the three classical unitary ensembles—GUE, LUE, and JUE—admits two complementary exact descriptions: (i) as Fredholm determinants of their orthogonal-polynomial correlation kernels and (ii) as isomonodromic τ -functions governed by Painlevé equations. For finite n , the associated Jimbo–Miwa–Okamoto σ -forms are P_{IV} (GUE), P_{V} (LUE), and P_{VI} (JUE); under soft- or hard-edge scalings these degenerate to P_{II} or P'_{III} descriptions of the Tracy–Widom and hard-edge laws [1, 2, 4].

It is well known among random matrix theorists (for example Folkmar Bornemann) that the Fredholm determinant is a more numerically stable and accurate way to compute the CDF of the largest eigenvalue for GUE, LUE, JUE than direct Painlevé integration. The aim of this paper is not to improve on Fredholm methods, but to see to what extent one can numerically recover the *correct* Painlevé solution from finite- n data and how unstable this reconstruction is. Numerically, we verify the equality between the Fredholm- and Painlevé-based CDFs by combining (a) high-accuracy Nyström discretizations of the finite- n Fredholm determinants [5] with (b) an anchored, branch-locked integration of the σ -form ODEs, where anchors are extracted from local least-squares fits to $\log \det(I - K)$. Our results confirm agreement across GUE/LUE/JUE with precision of $O(10^{-3})$ to $O(10^{-5})$ (occasionally $O(10^{-2})$) and illustrate the finite- n to scaling-limit transition. The theoretical connections to τ -functions and Virasoro constraints follow the framework of [2, 3].

1 Introduction

1.1 Preliminaries: ensembles, kernels, Fredholm determinants, Painlevé connections

We work with the classical unitary ensembles associated with Hermite, Laguerre, and Jacobi orthogonal polynomials [4]. In the Gaussian unitary ensemble (GUE) the eigenvalues are supported on \mathbb{R} with weight $w_H(x) = e^{-x^2}$. In the Laguerre unitary ensemble (LUE) the support is $[0, \infty)$ and the weight is $w_L(x) = x^\alpha e^{-x}$ with $\alpha > -1$. In the Jacobi unitary ensemble (JUE) the support is $(-1, 1)$ and the weight is $w_J(x) = (1 - x)^b(1 + x)^a$ with $a, b > -1$.

For each ensemble we write $\{\phi_k\}_{k \geq 0}$ for the orthonormal polynomial functions

$$\phi_k(x) = p_k(x)\sqrt{w(x)}, \quad \int \phi_k(x)\phi_\ell(x) dx = \delta_{k\ell},$$

where p_k is the orthonormal polynomial (Hermite, Laguerre, Jacobi) for the corresponding weight w .

The eigenvalues form a determinantal point process with m -point correlations

$$\rho_m(x_1, \dots, x_m) = \det[K^{(n)}(x_i, x_j)]_{i,j=1}^m,$$

where the finite- n correlation kernel is the orthogonal projection

$$K^{(n)}(x, y) = \sum_{k=0}^{n-1} \phi_k(x) \phi_k(y).$$

For numerical work we use the Christoffel–Darboux (CD) representation together with a diagonal fallback:

$$K^{(n)}(x, y) = \frac{\gamma_n(\phi_{n-1}(x)\phi_n(y) - \phi_n(x)\phi_{n-1}(y))}{x - y}, \quad K^{(n)}(x, x) = \sum_{k=0}^{n-1} \phi_k(x)^2,$$

with ensemble-dependent constants γ_n ; see [4, Ch. 2–5].

If B is a Borel set in the support and

$$(\mathsf{K}f)(x) = \int_B K^{(n)}(x, y) f(y) dy \quad \text{on } L^2(B),$$

then the probability that B contains no eigenvalue is a Fredholm determinant

$$E(B) = \det(I - \mathsf{K})_{L^2(B)}.$$

Taking B to be the one-sided interval at the upper edge gives the largest-eigenvalue CDFs:

$$\text{GUE: } F_n(s) = \det(I - \mathsf{K})_{(s, \infty)}, \quad \text{LUE: } F_{n,\alpha}(s) = \det(I - \mathsf{K})_{(s, \infty)}, \quad \text{JUE: } F_{n,a,b}(s) = \det(I - \mathsf{K})_{(s, 1)}.$$

We evaluate these determinants numerically via Nyström discretization [5]. For a quadrature rule $\{t_i, w_i\}_{i=1}^N$ on B we form the symmetric matrix

$$A_{ij} = \sqrt{w_i} K^{(n)}(t_i, t_j) \sqrt{w_j}, \quad F = \det(I - A) = \exp\left(\sum_{j=1}^N \log \lambda_j\right),$$

where $\{\lambda_j\}$ are the eigenvalues of $I - A$.

These Fredholm determinants are also isomonodromic τ -functions and satisfy Painlevé equations with ensemble-specific parameters [2, 3]. For finite n the largest-eigenvalue gaps are described by a σ -form of P_{IV} for GUE, a σ -form of P_{V} for LUE, and a σ -form of P_{VI} for JUE. At the soft edge these reduce to P_{II} (Tracy–Widom), while hard-edge scalings produce P'_{III} (Bessel kernel) [1, 2, 4]. One central theme of this paper is that, although these ODE characterizations are exact, the corresponding numerical IVPs are highly unstable and must be locked to the Fredholm side.

1.2 Finite- n P_{IV} for the GUE gap

Let F_n denote the finite- n GUE largest-eigenvalue distribution

$$F_n(s) := \mathbb{P}(\lambda_{\max} \leq s),$$

for the $n \times n$ GUE with weight e^{-x^2} . Equivalently,

$$F_n(s) = \mathbb{P}(\lambda_{\max} \leq s) = \mathbb{P}(\text{no eigenvalues lie in } (s, \infty)).$$

Following Forrester and Witte [2], write $E_n(0; (s, \infty))$ for the probability that (s, ∞) is free of eigenvalues. Their analysis (see Eq. (1.4)–(1.7) of [2]) shows that there is a distinguished function $R_n(s)$ such that

$$F_n(s) = E_n(0; (s, \infty)) = \exp\left(-\int_s^\infty R_n(t) dt\right), \quad (1)$$

and R_n satisfies the Jimbo–Miwa–Okamoto σ –form of P_{IV} :

$$(R_n''(s))^2 = 4(s R_n'(s) - R_n(s))^2 - 4(R_n'(s))^2(R_n'(s) + 2n). \quad (2)$$

The large- s behaviour is fixed by the Hermite-kernel tail:

$$R_n(s) \sim \frac{2^{n-1}}{\sqrt{\pi}(n-1)!} s^{2n-2} e^{-s^2}, \quad s \rightarrow +\infty. \quad (3)$$

Define the logarithmic derivative

$$\sigma_n(s) := \frac{d}{ds} \log F_n(s). \quad (4)$$

Differentiating (1) and using $\frac{d}{ds} \int_s^\infty R_n(t) dt = -R_n(s)$ gives

$$\sigma_n(s) = \frac{d}{ds} \log F_n(s) = R_n(s). \quad (5)$$

Thus the Forrester–Witte function R_n is exactly the logarithmic derivative of F_n .

Combining (2) and (5) yields the σ –form P_{IV} equation for σ_n .

Theorem 1 (Jimbo–Miwa–Okamoto σ –form for the finite- n GUE). *Let $F_n(s) = \mathbb{P}(\lambda_{\max} \leq s)$ be the largest-eigenvalue CDF of the $n \times n$ GUE with weight e^{-x^2} , and define σ_n by (4). Then:*

(i) σ_n satisfies the Jimbo–Miwa–Okamoto σ –form

$$(\sigma_n''(s))^2 = 4(s \sigma_n'(s) - \sigma_n(s))^2 - 4(\sigma_n'(s))^2(\sigma_n'(s) + 2n). \quad (6)$$

(ii) As $s \rightarrow +\infty$ one has

$$\sigma_n(s) \sim \frac{2^{n-1}}{\sqrt{\pi}(n-1)!} s^{2n-2} e^{-s^2}, \quad (7)$$

so in particular $\sigma_n(s) \rightarrow 0$.

(iii) Conversely, any smooth solution σ_n of (6) with asymptotics (7) reconstructs the CDF via

$$F_n(s) = \exp\left(\int_{s_0}^s \sigma_n(u) du\right), \quad \lim_{s \rightarrow +\infty} F_n(s) = 1, \quad (8)$$

for any reference point s_0 .

Remark 1. Equation (6) is the special case $a = 0$ of the general σ – P_{IV} satisfied by the spectral averages $\tilde{E}_N(\lambda; a)$ in Forrester–Witte [2, Eq. (1.9), Eq. (4.15)], after identifying $\sigma_n(s)$ with $U_N(s; 0)$ in their notation and setting $N = n$.

For completeness we recall the relation between the σ –form (6) and the usual P_{IV}

$$y'' = \frac{(y')^2}{2y} + \frac{3}{2}y^3 + 4xy^2 + 2(x^2 - \alpha)y + \frac{\beta}{y}, \quad (9)$$

in Okamoto’s Hamiltonian formulation. Introduce canonical coordinates $q(t), p(t)$ and the Hamiltonian

$$H(t; q, p) = (2p - q - 2t)pq - 2\alpha_1 p - \alpha_2 q, \quad (10)$$

where $(\alpha_0, \alpha_1, \alpha_2)$ satisfy $\alpha_0 + \alpha_1 + \alpha_2 = 1$. Hamilton’s equations are

$$\begin{aligned} q' &= q(4p - q - 2t) - 2\alpha_1, \\ p' &= 2p(q + t - p) + \alpha_2. \end{aligned} \quad (11)$$

Eliminating p yields (9) with parameters (α, β) linear in $(\alpha_0, \alpha_1, \alpha_2)$. For the GUE spectral averages $\tilde{E}_N(\lambda; a)$ one finds [2, Eq. (4.10), Eq. (4.15), Eq. (4.46)–(4.47)]

$$\alpha_0 = 1 + N + a, \quad \alpha_1 = -a, \quad \alpha_2 = -N.$$

In our largest-eigenvalue problem ($a = 0, N = n$) this becomes

$$\alpha_0 = 1 + n, \quad \alpha_1 = 0, \quad \alpha_2 = -n,$$

and (9) has $(\alpha, \beta) = (2n + 1, 0)$. The logarithmic derivative σ_n is an affine transform of the Hamiltonian:

$$\sigma_n(s) = U_n(s; 0) = H(s; q_n(s), p_n(s)) + (\text{explicit affine term}), \quad (12)$$

where (q_n, p_n) solve (11). The precise affine term, recorded in [2], plays no role numerically because it disappears from the σ -form.

1.3 Edge limit: from P_{IV} to P_{II} (Tracy–Widom)

At the upper edge $\sqrt{2n}$ set

$$s = \sqrt{2n} + x n^{1/6}, \quad t = \sqrt{2n} + y n^{1/6}.$$

Then, uniformly for (x, y) in compact sets,

$$n^{1/6} K_{\text{H}}^{(n)}(s, t) \longrightarrow K_{\text{Ai}}(x, y) = \frac{\text{Ai}(x)\text{Ai}'(y) - \text{Ai}'(x)\text{Ai}(y)}{x - y}.$$

Consequently, the soft-edge limit of the largest-eigenvalue CDF exists:

$$F_2(x) := \lim_{n \rightarrow \infty} F_n(\sqrt{2n} + x n^{-1/6}) = \det_{L^2([x, \infty))}(I - K_{\text{Ai}}). \quad (13)$$

Let q be the Hastings–McLeod solution of P_{II}

$$q''(x) = x q(x) + 2q(x)^3, \quad q(x) \sim \text{Ai}(x) \quad (x \rightarrow +\infty). \quad (14)$$

This solution is real, pole-free on \mathbb{R} , and behaves like $q(x) \sim \sqrt{-x/2}$ as $x \rightarrow -\infty$. Defining

$$F_2(x) = \exp \left[- \int_x^\infty (t - x) q(t)^2 dt \right], \quad (15)$$

Tracy and Widom showed [1] that the function F_2 in (15) coincides with the Fredholm determinant in (13). Thus F_2 is the limiting distribution of the scaled GUE largest eigenvalue and admits both a Fredholm and a Painlevé representation.

For finite n , the map $F_n \mapsto \sigma_n = \frac{d}{ds} \log F_n$ solves (6), and integrating (8) recovers F_n . Under soft-edge scaling, F_n converges to F_2 , which in turn satisfies both the Airy-kernel Fredholm representation (13) and the Painlevé–II representation (15). One can therefore track the finite- n GUE edge all the way to the universal Tracy–Widom regime through a chain of Painlevé equations (P_{IV} → P_{II}) and kernels (Hermite → Airy).

1.4 Finite- N LUE: Fredholm determinants and σ –PV

For $a > -1$, the LUE consists of $N \times N$ Hermitian positive-definite matrices with joint eigenvalue density

$$\frac{1}{Z_{N,a}} \prod_{1 \leq i < j \leq N} |\lambda_i - \lambda_j|^2 \prod_{i=1}^N \lambda_i^a e^{-\lambda_i} \mathbf{1}_{(0,\infty)}(\lambda_i) d\lambda_i.$$

Let $\{p_k\}$ be orthonormal Laguerre polynomials for $w(x) = x^a e^{-x}$ and set $\varphi_k(x) := p_k(x) w(x)^{1/2}$. The finite- N Laguerre kernel is the CD kernel

$$K_N^{(L)}(x, y) := \sum_{k=0}^{N-1} \varphi_k(x) \varphi_k(y) = \frac{\gamma_{N-1}}{\gamma_N} \frac{\varphi_N(x) \varphi_{N-1}(y) - \varphi_{N-1}(x) \varphi_N(y)}{x - y},$$

with the usual normalization constants γ_k .

The largest-eigenvalue CDF is the one-sided gap probability

$$F_N^{(L)}(s) = \mathbb{P}(\lambda_{\max} < s) = \det_{L^2((s, \infty))}(I - K_N^{(L)}),$$

where $(K_N^{(L)} f)(x) = \int_s^\infty K_N^{(L)}(x, y) f(y) dy$.

Following [7, 8], it is convenient to introduce the generating function

$$E_{N,2}^{(L)}((0, t); \xi) := \det_{L^2((0, t))}(I - \xi K_N^{(L)}),$$

for which there is a Painlevé–V τ –function $\tau_V(t)$ such that

$$E_{N,2}^{(L)}((0, t); \xi) = t^{(a+\mu)N+N^2} \tau_V(t) \Big|_{\nu_0=0, \nu_1=-\mu, \nu_2=N+a, \nu_3=N}.$$

Writing

$$\sigma_N^{(L)}(t) := \frac{d}{dt} \log E_{N,2}^{(L)}((0, t); 1),$$

one finds that $\sigma_N^{(L)}$ solves the Jimbo–Miwa–Okamoto σ –form of PV with parameters $(\nu_0, \nu_1, \nu_2, \nu_3) = (0, 0, N+a, N)$. The analytic behaviour at $t \rightarrow 0^+$ is fixed by the LUE one-point function and singles out the random-matrix branch. At the hard edge $t \sim O(N^{-1})$ one recovers P'_{III} ; at the soft edge, after the usual centering and $N^{1/3}$ scaling, one again finds P_{II} and Tracy–Widom.

1.5 Finite- N JUE: Fredholm determinants and σ –P_{VI}

For $a, b > -1$, the JUE has eigenvalue density on $(-1, 1)$

$$\frac{1}{\tilde{Z}_{N,a,b}} \prod_{1 \leq i < j \leq N} |\lambda_i - \lambda_j|^2 \prod_{i=1}^N (1 - \lambda_i)^a (1 + \lambda_i)^b \mathbf{1}_{(-1,1)}(\lambda_i) d\lambda_i.$$

Write $\{P_k\}$ for orthonormal Jacobi polynomials for $w(x) = (1-x)^a (1+x)^b$ and set $\psi_k(x) := P_k(x) w(x)^{1/2}$. The finite- N Jacobi kernel is

$$K_N^{(J)}(x, y) := \sum_{k=0}^{N-1} \psi_k(x) \psi_k(y) = \frac{\kappa_{N-1}}{\kappa_N} \frac{\psi_N(x) \psi_{N-1}(y) - \psi_{N-1}(x) \psi_N(y)}{x - y}.$$

For $t \in (-1, 1)$ and $\xi \in \mathbb{C}$,

$$E_{N,2}^{(J)}((t, 1); \xi) := \det_{L^2((t, 1))}(I - \xi K_N^{(J)}),$$

and

$$F_N^{(J)}(s) := \mathbb{P}(\lambda_{\max} < s) = E_{N,2}^{(J)}((s, 1); 1).$$

There is a Painlevé–VI τ –function $\tau_{VI}(t)$ whose σ –function

$$\sigma_{VI}(t) := t(t-1) \frac{d}{dt} \log \tau_{VI}(t)$$

solves the σ –form of P_{VI} with parameters

$$v_1 = v_3 = N + \frac{a+b}{2}, \quad v_2 = \frac{a+b}{2}, \quad v_4 = \frac{b-a}{2},$$

see [7, 9]. The logarithmic derivative of the JUE gap can be identified with σ_{VI} up to an affine transform. After rescaling near the endpoints $t = \pm 1$ one obtains the Bessel hard-edge limits, and in the double-Wishart (MANOVA) soft-edge regime one recovers the Tracy–Widom F_2 law [7, 11].

2 Numerical verification via Painlevé II

We begin with the simplest setting, where the Painlevé description is well conditioned and can serve as a reference. We solve (14) with boundary data approximating $\text{Ai}(x)$ at large positive x and then evaluate F_2 via (15). Independently, we compute the Fredholm determinant representation (13) using a Nyström method with Gauss–Legendre quadrature.

2.1 Numerical methods

We briefly summarize the schemes used to evaluate the Tracy–Widom GUE distribution $F_2(x)$ on a real interval $[x_{\min}, x_{\max}]$.

For the Painlevé II side we rewrite P_{II} as the first-order system

$$q'(x) = p(x), \quad p'(x) = xq(x) + 2q(x)^3$$

for $u = (q, p)^{\top}$ and approximate the asymptotic condition at $+\infty$ by prescribing

$$q(T_0) = \text{Ai}(T_0), \quad q'(T_0) = \text{Ai}'(T_0)$$

at some large T_0 . We then integrate backwards from T_0 down to x_{\min} with a high-order explicit Runge–Kutta method (in the implementation, a 7th-order Verner scheme with adaptive stepsize). The solver provides a dense representation of $q(x)$ which we sample on a uniform grid $x_k \in [x_{\min}, x_{\max}]$.

Given sampled values $q(x_k)$ we approximate

$$\log F_2(x) = - \int_x^{\infty} (t - x) q(t)^2 dt.$$

On the grid we compute cumulative trapezoidal sums from right to left,

$$I_0(x_k) \approx \int_{x_k}^{x_{\max}} q(t)^2 dt, \quad I_1(x_k) \approx \int_{x_k}^{x_{\max}} t q(t)^2 dt,$$

and approximate the tail beyond T_0 by replacing q with Ai and integrating numerically. This yields

$$\log F_2(x_k) \approx - (I_1(x_k) - x_k I_0(x_k)) - \left(\int_{T_0}^{\infty} t \text{Ai}(t)^2 dt - x_k \int_{T_0}^{\infty} \text{Ai}(t)^2 dt \right),$$

and $F_2(x_k)$ is obtained by exponentiation.

On the Fredholm side we discretize the Airy kernel

$$K_{\text{Ai}}(s, t) = \frac{\text{Ai}(s)\text{Ai}'(t) - \text{Ai}'(s)\text{Ai}(t)}{s - t}, \quad K_{\text{Ai}}(s, s) = \text{Ai}'(s)^2 - s \text{Ai}(s)^2,$$

on (x, ∞) via Nyström. We map (x, ∞) to $(0, 1)$ by $t = x + z/(1 - z)$ and pull back an N -point Gauss–Legendre rule $\{z_j, w_j\}$. Denoting $t_j = x + z_j/(1 - z_j)$ and $\omega_j = w_j/(1 - z_j)^2$, we form the symmetric matrix

$$A_{ij}(x) = \sqrt{\omega_i} K_{\text{Ai}}(t_i, t_j) \sqrt{\omega_j},$$

compute the eigenvalues $\lambda_1, \dots, \lambda_N$ of $I - A(x)$, and set

$$F_2(x) \approx \exp \left(\sum_{j=1}^N \log \lambda_j \right).$$

We repeat this for the same x -grid as on the Painlevé side.

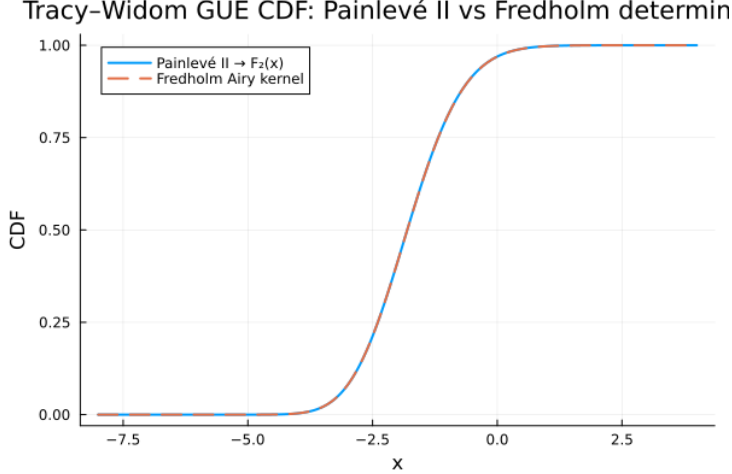


Figure 1: Tracy–Widom GUE CDF $F_2(x)$ from the Painlevé II solution (solid) and the Airy-kernel Fredholm determinant (dashed).

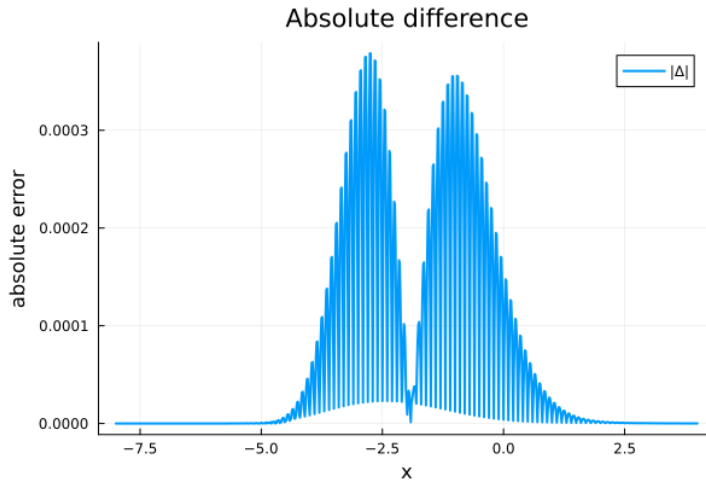


Figure 2: Absolute difference between the two numerical evaluations of $F_2(x)$.

2.2 Results

Figure 1 shows the Tracy–Widom CDF $F_2(x)$ computed from Painlevé II and from the Airy-kernel Fredholm determinant on $x \in [-8, 4]$. The curves are visually indistinguishable. The absolute difference in Figure 2 stays below 3×10^{-4} , consistent with the quadrature and ODE tolerances for $N = 80$ Nyström nodes.

2.3 A brief comment on conditioning

The Painlevé II computation is intrinsically ill conditioned when formulated as a backward IVP from T_0 . Linearization around the Hastings–McLeod solution reveals an unstable direction whose amplification factor between T_0 and the bulk is of order $\exp(c(T_0^{3/2} - x^{3/2}))$ for some $c > 0$, so double-precision roundoff at T_0 is magnified to roughly 10^{-4} near $x \approx 0$. Moreover we impose only the leading Airy asymptotics at T_0 and approximate the tails of the integral. For our purposes this four-digit accuracy is acceptable and provides a clean benchmark against which to compare the much more fragile finite- n Painlevé IV calculations. A broader discussion of numerical conditioning and limitations is given in Section 8.

3 Numerical verification of P_{IV} for finite- n GUE

We now turn to the main object of interest: the finite- n GUE gap and its σ - P_{IV} description. This is where numerical instability becomes serious and where our Fredholm-anchored σ -form integration comes into play.

3.1 Direct IVP for the σ -form and its failure

Figure 3 illustrates what happens if one simply treats (6) as an initial-value problem. We choose a base point $s_0 \approx \sqrt{2n}$, estimate $\sigma_n(s_0)$ and $\sigma'_n(s_0)$ from a local polynomial fit to $\log F_n$ computed via the Fredholm determinant, and then integrate (6) forward and backward in s with a standard ODE solver.

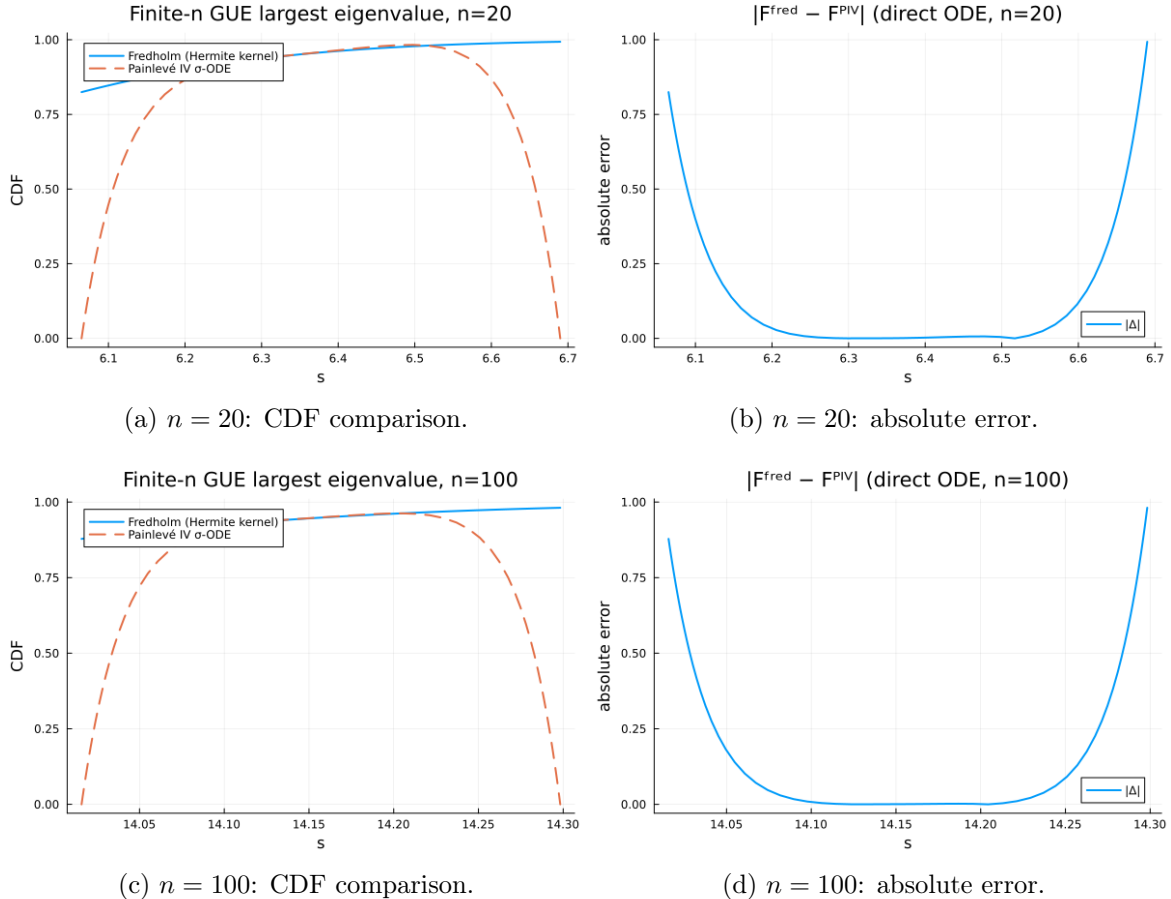


Figure 3: Direct ODE solutions of the P_{IV} σ -equation compared with the finite- n GUE Fredholm determinant.

The σ - P_{IV} equation is second order and second degree with movable poles, and the random-matrix solution corresponding to F_n is a very special trajectory. The Cauchy data extracted at s_0 are only approximate, and tiny perturbations tend to push the ODE onto a different Painlevé branch that typically develops a real pole within the s -window of interest. Numerically this shows up as the adaptive solver repeatedly shrinking the timestep until it reaches machine precision and aborts, and as non-monotone, bump-shaped curves $F_{\text{PIV}}(s)$ which match the Fredholm CDF only in a small neighbourhood of s_0 before bending back down toward zero at both ends.

In other words, direct shooting from a single approximate anchor is an ill-posed strategy in standard double precision: the IVP is extremely sensitive to initial data, blind to the requirement

that F_n be a CDF, and prone to encountering movable poles. This motivates the anchored and branch-locked approach described next.

3.2 Numerical methods (ODE-based σ -form integration)

This subsection describes the prototype algorithm and is kept essentially unchanged, since its structure is reused in the later LUE and JUE experiments.

We now describe a variant of the above scheme in which the PIV σ -equation is integrated between anchors using a standard ODE solver, rather than an explicit hand-crafted predictor–corrector update. The Fredholm determinant side and the extraction of anchor data are unchanged; only the propagation mechanism between anchors is modified.

3.2.1 ODE formulation with signed branch

Recall the PIV σ -equation for the finite- n largest-eigenvalue CDF:

$$(\sigma_n''(s))^2 = 4(s\sigma'_n(s) - \sigma_n(s))^2 - 4(\sigma'_n(s))^2(\sigma'_n(s) + 2n),$$

which we write concisely as

$$(\sigma_n''(s))^2 = R(s, \sigma_n(s), \sigma'_n(s)), \quad R(s, \sigma, \sigma') := 4(s\sigma' - \sigma)^2 - 4(\sigma')^2(\sigma' + 2n).$$

Since the equation is of second degree in σ_n'' , it determines σ_n'' only up to a sign:

$$\sigma_n''(s) = \pm \sqrt{R(s, \sigma_n(s), \sigma'_n(s))}.$$

To integrate numerically we rewrite the problem as a first-order system in the state vector $u = (\sigma_n, \sigma'_n)$:

$$\frac{d}{ds} \begin{pmatrix} \sigma_n(s) \\ \sigma'_n(s) \end{pmatrix} = \begin{pmatrix} \sigma'_n(s) \\ \sigma''_n(s) \end{pmatrix} = \begin{pmatrix} \sigma'_n(s) \\ \operatorname{sgn}_j \sqrt{R(s, \sigma_n(s), \sigma'_n(s))} \end{pmatrix},$$

where $\operatorname{sgn}_j \in \{-1, +1\}$ is a fixed branch-sign parameter on each anchor interval $[s^{(j+1)}, s^{(j)}]$ (see below). Thus, once sgn_j is chosen, the right-hand side is single-valued and we obtain a well-posed first-order ODE system $u'(s) = f(s, u(s); n, \operatorname{sgn}_j)$, which we solve with a high-order explicit Runge–Kutta method with adaptive stepsize control.

For numerical robustness we include a safeguard when the radicand becomes non-positive: if $R(s, \sigma, \sigma') \leq 0$ we set the second component of $f(s, u)$ to zero, effectively freezing σ_n'' at that point. In practice this only occurs deep in the tails, where $F_n(s)$ is extremely close to 0 or 1 and the overall error is dominated by the Fredholm truncation.

3.2.2 Anchor data and branch selection on each interval

We fix a spectral window

$$[s_{\min}, s_{\max}] = [\sqrt{2n} - W, \sqrt{2n} + W],$$

with $W \approx 3$, and choose a descending sequence of anchor points $s^{(1)} > s^{(2)} > \dots > s^{(N_{\text{anc}})}$ uniformly in $[s_{\min}, s_{\max}]$. At each anchor $s^{(j)}$ we compute $F_n(s)$ on a short symmetric stencil and fit a degree-4 polynomial to

$$g(s) := \log F_n(s).$$

Writing

$$g(s^{(j)} + u) \approx c_0^{(j)} + c_1^{(j)}u + c_2^{(j)}u^2 + c_3^{(j)}u^3 + c_4^{(j)}u^4,$$

we recover the approximate Cauchy data

$$F_n(s^{(j)}) \approx e^{c_0^{(j)}}, \quad \sigma_n(s^{(j)}) \approx c_1^{(j)}, \quad \sigma'_n(s^{(j)}) \approx 2c_2^{(j)}, \quad \sigma''_n(s^{(j)}) \approx 6c_3^{(j)}.$$

These values are then used to define both the initial condition and the branch sign on the interval to the left of $s^{(j)}$.

For each interval $[s^{(j+1)}, s^{(j)}]$ we set

$$u^{(j)}(s^{(j)}) := (\sigma_n(s^{(j)}), \sigma'_n(s^{(j)})) \approx (c_1^{(j)}, 2c_2^{(j)}),$$

and choose

$$\text{sgn}_j := \begin{cases} +1, & \text{if } |\sigma''_n(s^{(j)})| \leq \varepsilon_{\text{init}}, \\ \text{sign}(\sigma''_n(s^{(j)})), & \text{otherwise,} \end{cases}$$

where $\sigma''_n(s^{(j)}) \approx 6c_3^{(j)}$ and $\varepsilon_{\text{init}} > 0$ is a small threshold. This ensures that each interval carries a constant branch sign tied to the Fredholm-based estimate of σ''_n at its right endpoint while preventing the integration from being trapped near $\sigma''_n \equiv 0$ when the third derivative is numerically small.

3.2.3 ODE integration between anchors and reprojection

We introduce a global descending grid

$$s_1 = s_{\max} > s_2 > \dots > s_{N_{\text{grid}}} = s_{\min}$$

covering the same spectral window and partition it by anchor intervals. On each interval $[s^{(j+1)}, s^{(j)}]$ we form the list of grid points with $s_k \in [s^{(j+1)}, s^{(j)}]$ and integrate

$$u'(s) = f(s, u(s); n, \text{sgn}_j),$$

with initial condition $u(s^{(j)}) = u^{(j)}(s^{(j)})$, evaluating the solution at these grid points. This yields values $(\sigma_n(s_k), \sigma'_n(s_k))$ with local error controlled by the usual ODE tolerances.

At the left endpoint $s^{(j+1)}$ we re-anchor the solution by overwriting the propagated values with the Fredholm-based Cauchy data:

$$\sigma_n(s^{(j+1)}) \leftarrow c_1^{(j+1)}, \quad \sigma'_n(s^{(j+1)}) \leftarrow 2c_2^{(j+1)}.$$

The corresponding $\sigma''_n(s^{(j+1)})$ is retained only for determining the next branch sign. This reprojection prevents the accumulation of drift and keeps the ODE solution consistent with the Hermite-kernel Fredholm determinant at every anchor.

3.2.4 Reconstruction of the CDF

Once $\sigma_n(s_k)$ has been computed on the global grid, we reconstruct $F_n(s_k)$ from

$$\frac{d}{ds} \log F_n(s) = \sigma_n(s)$$

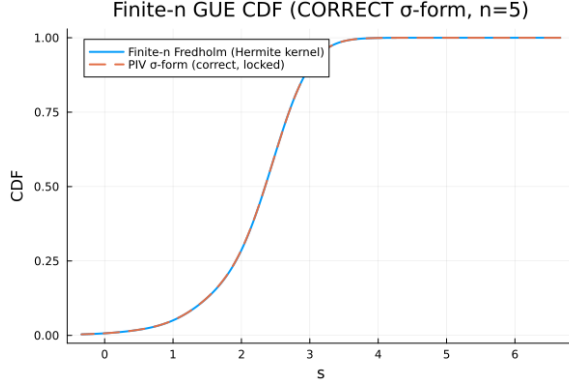
by trapezoidal integration from a base anchor s_0 with known $F_n(s_0)$:

$$\log F_n(s_k) \approx \log F_n(s_0) + \sum_{\ell: s_\ell \in [s_0, s_k]} \frac{\sigma_n(s_\ell) + \sigma_n(s_{\ell+1})}{2} (s_{\ell+1} - s_\ell).$$

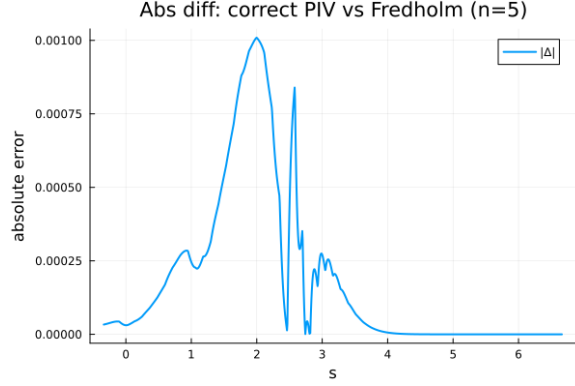
We then set $F_n(s_k) = \exp(\log F_n(s_k))$. This gives a numerical CDF which agrees with the Hermite Fredholm determinant to high accuracy and in which the PIV σ -form acts as a dynamical constraint between sparse Fredholm anchors.

3.3 Results and analysis

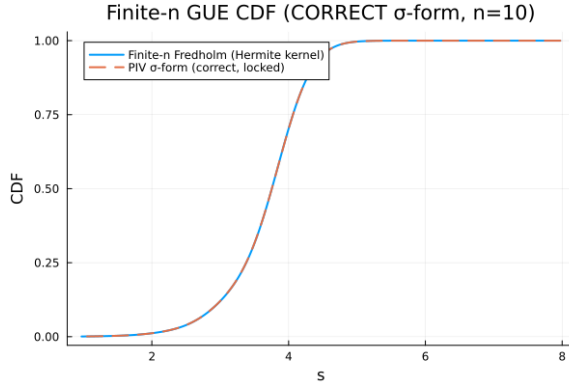
Figures 4a–8b show the comparison between the anchored P_{IV} solution and the Hermite Fredholm determinant for $n = 5, 10, 20, 100, 500$. In each case we display the CDF and the absolute error over a window centered at $\sqrt{2n}$.



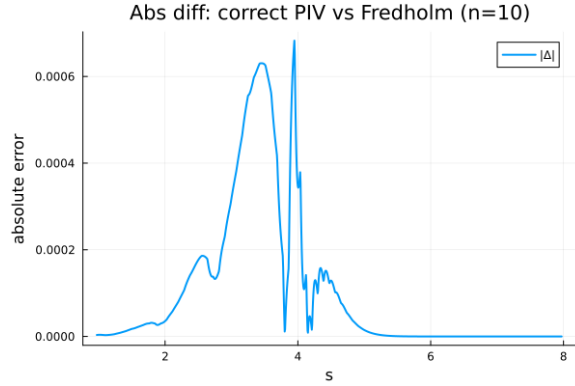
(a) $n = 5$: CDF.



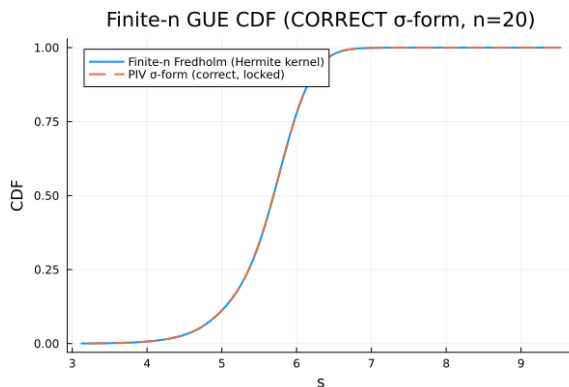
(b) $n = 5$: absolute error.



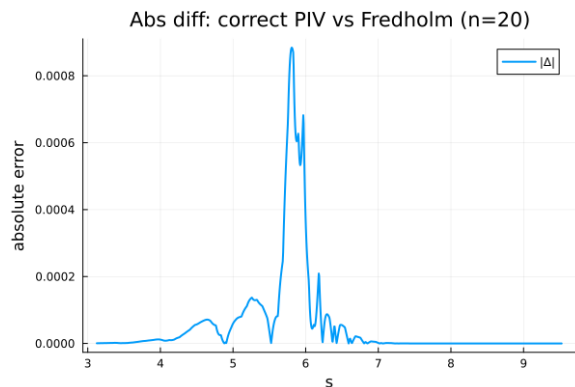
(a) $n = 10$: CDF.



(b) $n = 10$: absolute error.



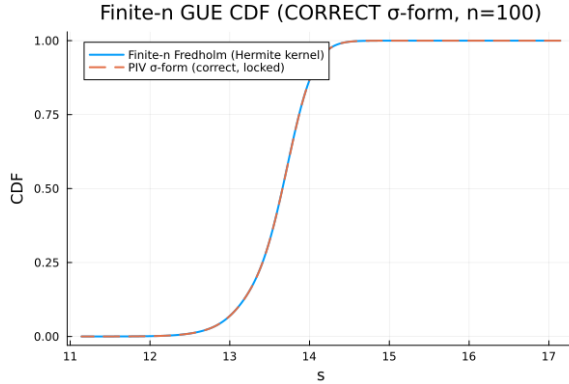
(a) $n = 20$: CDF.



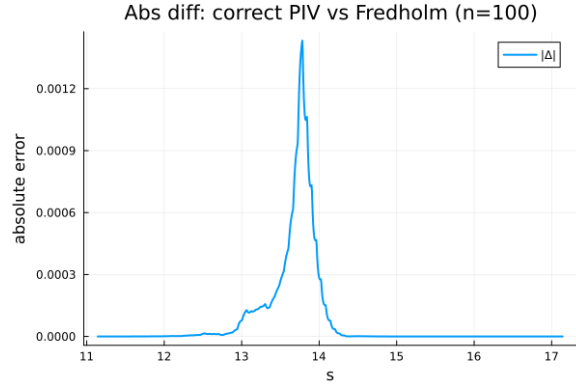
(b) $n = 20$: absolute error.

Table 1 summarizes the maximum absolute errors between the two methods and the corresponding spectral windows.

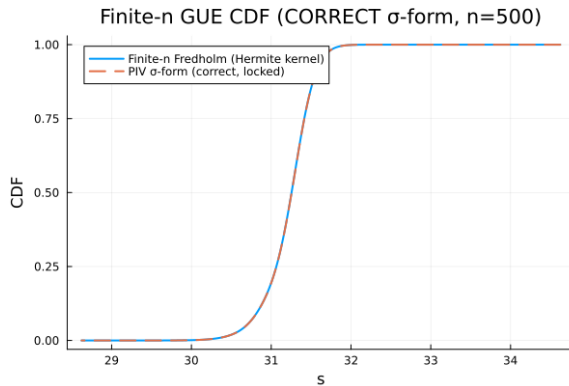
For n up to about 500 the anchored P_{IV} and Fredholm CDFs agree to roughly 10^{-3} in the transition region and much better in the tails. For very large n the fixed physical window $[s_{\min}, s_{\max}]$ sits far into the regime where $F_n(s)$ is already extremely close to 1, and both the Hermite basis and the Fredholm matrix become ill conditioned in double precision. At that



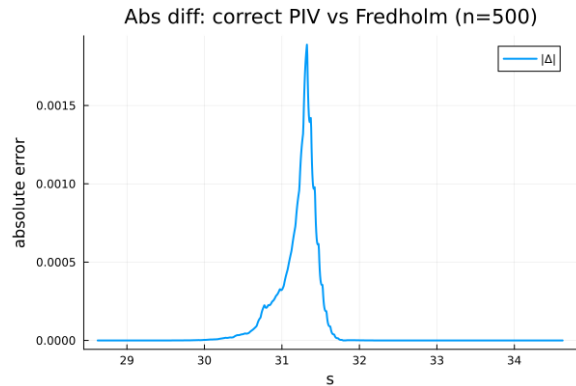
(a) $n = 100$: CDF.



(b) $n = 100$: absolute error.



(a) $n = 500$: CDF.



(b) $n = 500$: absolute error.

point the true error is dominated by underflow and cancellation, and the plots primarily reflect saturation effects rather than meaningful extra digits. Conceptually this is not a problem: for such n it is more natural to pass to the soft-edge scaling and use the stable P_{II}/F_2 description. A more systematic discussion of the global limitations of the anchored scheme is deferred to Section 8.

3.4 Large- n behaviour and interpretation

For moderate sizes the anchored P_{IV} computation behaves exactly as dictated by the theory: it recovers the finite- n GUE gap with a controlled discrepancy that is largest near the soft edge and negligible in the tails. As n increases, the natural soft-edge scale is

$$s = \mu(n) + \sigma(n)x, \quad \mu(n) = \sqrt{2n}, \quad \sigma(n) \asymp n^{-1/6},$$

so a fixed physical window $[\mu(n) - \Delta, \mu(n) + \Delta]$ corresponds to an x -window that grows with n . On the right half of this window the Tracy–Widom limit $F_2(x)$ is already extremely close to 1 when x is moderately positive, and double-precision arithmetic can no longer resolve small differences in $\log F_n$ or in the Nyström eigenvalues. The anchored P_{IV} solver then essentially returns a plateau at $F_n \approx 1$ with tiny numerical fluctuations. For the purposes of this paper we do not push beyond $n \approx 500$ in the finite- n GUE computations and treat the large- n regime via P_{II} and the Airy kernel instead.

n	Max error	Edge location	Window width
5	1.01×10^{-3}	$\sqrt{10} \approx 3.16$	7.0
10	6.83×10^{-4}	$\sqrt{20} \approx 4.47$	7.0
20	8.84×10^{-4}	$\sqrt{40} \approx 6.32$	6.4
100	1.43×10^{-3}	$\sqrt{200} \approx 14.14$	6.0
500	1.89×10^{-3}	$\sqrt{1000} \approx 31.62$	6.0

Table 1: Maximum absolute errors and problem parameters for the anchored P_{IV} method.

4 Painlevé VI for JUE and finite- N hard edges

4.1 Finite- N JUE gap and anchored P_{VI}

For the JUE we verify that the largest-eigenvalue CDF

$$F_N(s) = \det_{L^2(s,1)}(I - K_N)$$

agrees, for finite N , with the Painlevé VI description derived from the Jimbo–Miwa–Okamoto σ -form. The finite- N kernel K_N is constructed from orthonormal Jacobi functions ϕ_k as in Section 1.5. To approximate $F_N(s)$ we use a Gram-type Nyström method: map Gauss–Legendre nodes $z_i \in (-1, 1)$ to $t_i \in (s, 1)$, form the matrix $\Phi_{ik} = \sqrt{w_i^{(s)}} \phi_k(t_i)$, and compute

$$F_N^{(\text{Fred})}(s) \approx \det(I_N - G), \quad G = \Phi^\top \Phi.$$

On the Painlevé side we adopt the same philosophy as for P_{IV}. We work with the P_{VI} σ -form associated to the JUE gap and the corresponding second-order second-degree ODE for $f(t) = F_N^{(J)}(t; a, b, 0; 1)$. Introducing $g(t) = (1-t)f'(t)$ and the stretched variable $y = -\log(1-t)$, we obtain a first-order system for (f, g, t) in y , with $f''(t)$ recovered at each step from the algebraic σ -form. The two quadratic roots are disambiguated by a branch-locking rule exactly as in the P_{IV} case.

Anchors are now placed automatically in the y -variable: for each (N, a, b) we determine a window $[s_{\min}, s_{\max}]$ by solving $F_N^{(\text{Fred})}(s_{\min}) \approx 0.1$ and $F_N^{(\text{Fred})}(s_{\max}) \approx 1 - 10^{-8}$, then map this to $t \in [t_{\min}, t_{\max}]$ and $y \in [y_{\min}, y_{\max}]$. Uniformly spaced y_j are mapped back to s_j and used as anchors. At each s_j we extract $F_N(s_j)$ and its first two derivatives in s from a local least-squares fit to $\log F_N(s)$, convert these to $f(t_j)$, $f'(t_j)$, $f''(t_j)$, and launch a PVI integration segment in y until the next anchor, where we relock the solution.

As in the GUE case we find that the anchored P_{VI} solution reproduces the JUE Fredholm CDF with errors of size 10^{-3} – 10^{-2} in the transition region, relatively insensitive to N once the quadrature and anchor grids are chosen. Rather than repeating a detailed error discussion here, we refer to the hard-edge analysis below and to the global limitations in Section 8.

5 JUE hard-edge limits and Bessel kernels

We next check numerically that the Jacobi ensemble with weight $(1-x)^a(1+x)^b$ has Bessel hard-edge limits at both endpoints. Writing $F_N^{(J)}(t; a, b)$ for the finite- N gap probability, the theory predicts

$$E_{N,\text{right}}^{(a,b)}(s) := F_N^{(J)}\left(1 - \frac{s}{2N^2}; a, b\right) \longrightarrow E_{\text{hard}}^{(a)}(s),$$

$$E_{N,\text{left}}^{(a,b)}(s) := F_N^{(J)}\left(-1 + \frac{s}{2N^2}; a, b\right) = F_N^{(J)}\left(1 - \frac{s}{2N^2}; b, a\right) \longrightarrow E_{\text{hard}}^{(b)}(s),$$

where $E_{\text{hard}}^{(\alpha)}(s) = \det(I - K_{\text{Bes}}^{(\alpha)})_{L^2(0,s)}$ and $K_{\text{Bes}}^{(\alpha)}$ is the Bessel kernel of order α [4, 6, 7].

On the finite- N side we evaluate $F_N^{(J)}$ by Nyström discretization of the rank- N Jacobi kernel as before, now on $(t, 1)$ with t near ± 1 and t scaled as above. On the Bessel side we implement the standard off-diagonal formula

$$K_{\text{Bes}}^{(\alpha)}(x, y) = \frac{J_\alpha(\sqrt{x})\sqrt{y} J'_\alpha(\sqrt{y}) - J_\alpha(\sqrt{y})\sqrt{x} J'_\alpha(\sqrt{x})}{2(x - y)},$$

with the diagonal handled by a symmetric finite difference, and discretize on $(0, s)$ using Gauss-Legendre nodes. In both cases the eigenvalues of $I - A$ are used to compute $\log \det(I - A)$.

For the symmetric case $(a, b) = (0, 0)$ the left and right edges coincide. Table 2 reports the maximal absolute discrepancy over $s \in [0, 15]$ for $N = 20, 40, 80, 120, 300$.

Table 2: Maximum hard-edge error for $(a, b) = (0, 0)$: $\max_s |E_{N,\text{edge}}^{(0,0)}(s) - E_{\text{hard}}^{(0)}(s)|$ on $s \in [0, 15]$.

N	right edge max $ \Delta $	left edge max $ \Delta $
20	6.77×10^{-4}	6.77×10^{-4}
40	1.69×10^{-4}	1.69×10^{-4}
80	4.23×10^{-5}	4.23×10^{-5}
120	1.88×10^{-5}	1.88×10^{-5}
300	4.25×10^{-6}	4.25×10^{-6}

The error decreases rapidly with N and is already at the 10^{-6} level for $N = 300$. For asymmetric parameters the convergence is slightly slower but still robust. Table 3 lists the maximal errors for $N = 300$ and several (a, b) .

Table 3: Maximum hard-edge error at $N = 300$: $\max_s |E_{N,\text{edge}}^{(a,b)}(s) - E_{\text{hard}}^{(\alpha)}(s)|$ on $s \in [0, 15]$, where $\alpha = a$ at the right edge and $\alpha = b$ at the left edge.

(a, b)	edge	max $ \Delta $	Bessel order α
$(0, 0)$	right	4.25×10^{-6}	0
	left	4.25×10^{-6}	0
$(2, 0)$	right	4.03×10^{-3}	2
	left	2.45×10^{-3}	0
$(0, 3)$	right	3.66×10^{-3}	0
	left	2.88×10^{-3}	3
$(2, 3)$	right	1.01×10^{-2}	2
	left	4.82×10^{-3}	3

Figure 9 shows representative CDFs and error curves for the most asymmetric case $(a, b) = (2, 3)$ at $N = 300$. The finite- N JUE hard-edge statistics closely track the corresponding Bessel limits, with absolute errors of order 10^{-3} – 10^{-2} concentrated near the edge.

6 JUE soft edge and Tracy–Widom limit

Finally we test the JUE soft-edge scaling limit by Monte Carlo simulation of double-Wishart (MANOVA) matrices and comparison with the standardised Tracy–Widom F_2 law.

We simulate the largest eigenvalue of

$$\Theta = (A + B)^{-1}B,$$

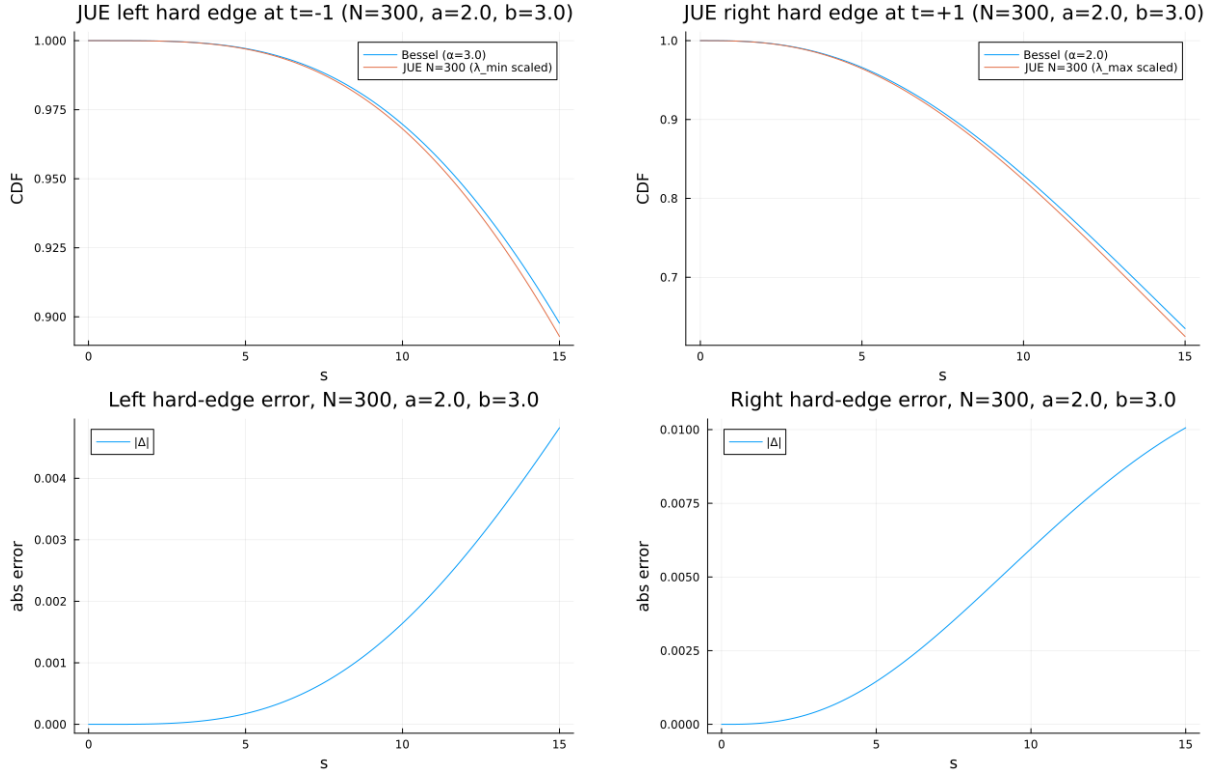


Figure 9: Hard-edge comparison for $(a, b) = (2, 3)$ at $N = 300$. Top: CDF of rescaled JUE extremal eigenvalues versus the Bessel hard-edge limit at the left (top left) and right (top right) edges. Bottom: corresponding absolute errors.

where $A \sim \text{CW}_N(I, n_1)$ and $B \sim \text{CW}_N(I, n_2)$ are independent complex Wishart matrices with $n_1 \approx 2N$, $n_2 \approx 3N$. The eigenvalues of Θ form a JUE on $(0, 1)$ with parameters determined by (N, n_1, n_2) , and λ_{\max} represents the JUE soft edge. For each $N \in \{100, 200, 400\}$ we generate M independent samples, estimate the empirical mean μ_N and standard deviation σ_N of λ_{\max} , and form standardised variables

$$z_m = \frac{\lambda_{\max}^{(m)} - \mu_N}{\sigma_N}.$$

The empirical CDF $F_N(z)$ is then compared on $[-4, 4]$ with the standardised Tracy–Widom CDF

$$F_2^{\text{std}}(z) := F_2(\mu_{F_2} + \sigma_{F_2} z),$$

where μ_{F_2} and σ_{F_2} are the numerically computed mean and standard deviation of F_2 from the Fredholm Airy kernel.

Table 4 summarises the results, including the scale-invariant quantity $\sigma_N N^{2/3}$ and the Kolmogorov distance

$$\Delta_N := \sup_{z \in [-4, 4]} |F_N(z) - F_2^{\text{std}}(z)|.$$

The products $\sigma_N N^{2/3}$ are slowly varying and remain of order 10^{-1} as N grows, consistent with the $N^{-2/3}$ soft-edge scale. The Kolmogorov distances Δ_N lie in the range $10^{-2} - 2 \times 10^{-2}$, which is compatible with the expected $O(N^{-2/3})$ finite- N bias and the $O(M^{-1/2})$ Monte Carlo fluctuations for $M \leq 5000$. In other words, at the level of accuracy accessible with these sample sizes the JUE soft edge behaves as predicted by the Tracy–Widom F_2 law.

N	M	$\mathbb{E}[\lambda_{\max}]$	$\text{sd}(\lambda_{\max})$	$\sigma_N N^{2/3}$	Δ_N on $[-4, 4]$
100	2000	0.94534	0.00346	0.07451	0.017
200	2000	0.94793	0.00211	0.07231	0.014
400	2000	0.94941	0.00125	0.06798	0.016
100	5000	0.94537	0.00348	0.07489	0.018
200	5000	0.94782	0.00214	0.07316	0.008
400	5000	0.94939	0.00128	0.06943	0.012

Table 4: Monte Carlo approximation of the JUE soft-edge law for $(N, n_1, n_2) \approx (N, 2N, 3N)$, compared with the standardised Tracy–Widom $F_2^{\text{std}}(z)$ on $[-4, 4]$.

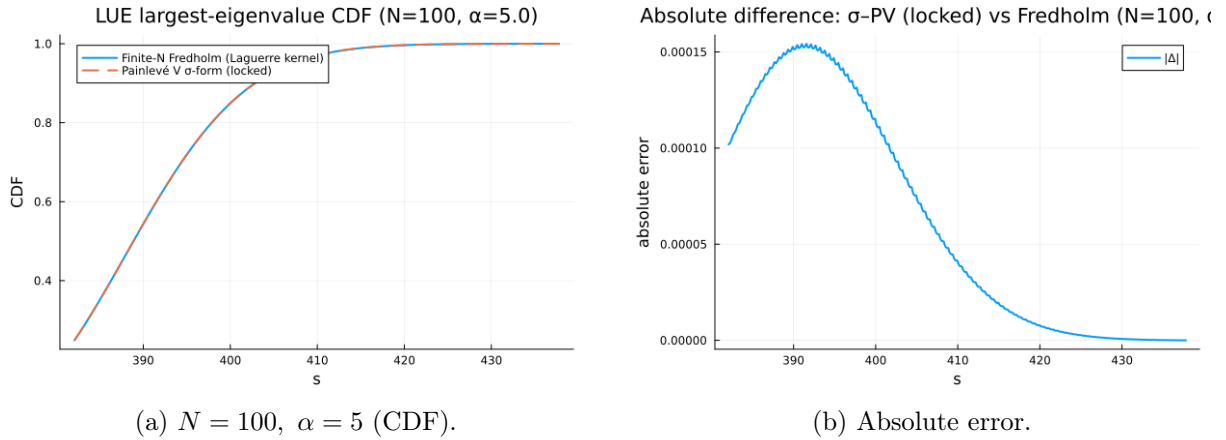


Figure 10: LUE: Fredholm vs. locked σ –PV (case 1).

7 LUE soft and hard edges via PV

7.1 Finite- N LUE and anchored σ –PV

For LUE we repeat the anchored σ –form strategy but now for the σ –PV equation described in Section 1.4. The orthonormal Laguerre functions are

$$\phi_k(x) = \frac{L_k^{(\alpha)}(x)}{\sqrt{h_k}} x^{\alpha/2} e^{-x/2}, \quad h_k = \frac{\Gamma(k + \alpha + 1)}{k!},$$

and the CD kernel K_N is built from ϕ_k with a diagonal fallback on $x = y$. We discretise (s, ∞) via Nyström on $[s, s + L]$ with M Gauss–Legendre nodes and form the symmetric matrix A as before. The CDF $F_N(s)$ is again computed as $\exp \sum_j \log \lambda_j$ from the eigenvalues of $I - A$.

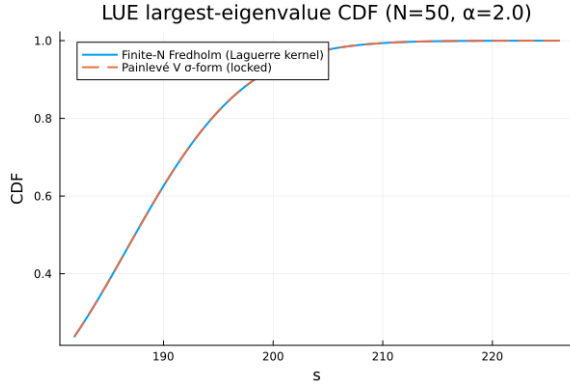
Anchors are placed near the soft edge, and local polynomial fits to $\log F_N$ provide estimates of σ and its first derivative; these fix the branch of the algebraic σ –PV equation for σ'' on each interval. The ODE between anchors is integrated with the same signed-branch and reprojection strategy as in the PIV case.

Figures 10–13 show representative comparisons between the LUE Fredholm CDF and the anchored σ –PV solution for four parameter choices. Table 5 summarises the maximum absolute discrepancy, which remains below 6×10^{-4} even for the smallest N considered.

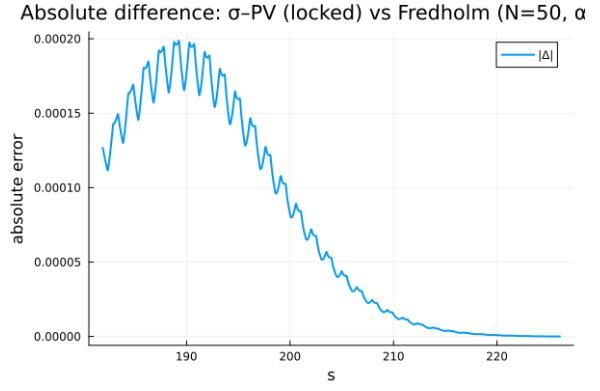
7.2 LUE hard and soft edges

The same finite- N Laguerre Fredholm machinery also allows us to reproduce the universal LUE hard-edge and soft-edge limits. At the hard edge we consider

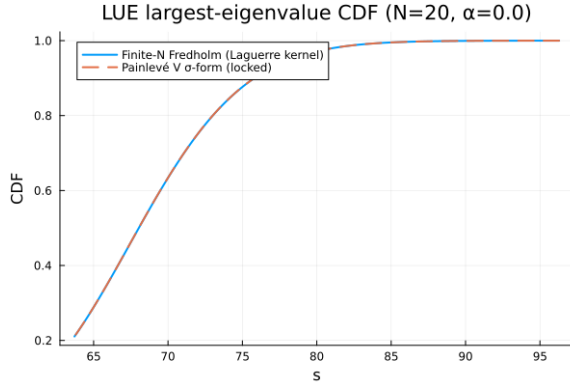
$$E_N^{(L)}((0, t); 1) = \det_{L^2((0, t))}(I - K_N^{(L)})$$



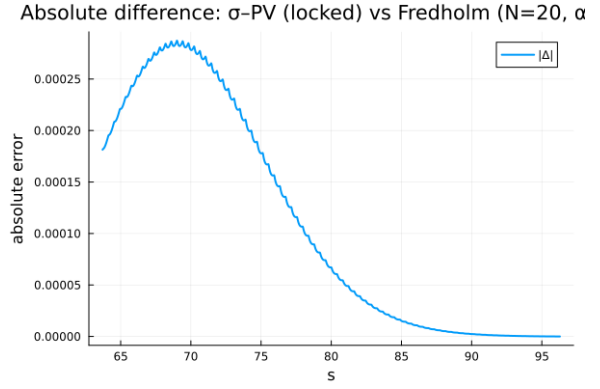
(a) $N = 50$, $\alpha = 2$ (CDF).



(b) Absolute error.



(a) $N = 20$, $\alpha = 0$ (CDF).



(b) Absolute error.

with $a = 0$ and scaling $t = s/(4N)$, and compare it to the Bessel gap $E_{\text{hard}}^{(0)}(s)$. The implementation is identical in spirit to the JUE hard-edge test: we discretise the Laguerre and Bessel kernels on $(0, t)$ and $(0, s)$, respectively, with Gauss–Legendre nodes and compare the determinants. For $N = 20, 40, 80$ we find maximal errors of $O(10^{-4})$, $O(10^{-5})$, and $O(10^{-5})$ respectively over $s \in [0.5, 10]$.

At the soft edge we study the largest-eigenvalue CDF $F_N^{(L)}(s)$ and compare its centred and scaled version with the Tracy–Widom F_2 law, now using fully deterministic Fredholm computations on both sides. We calibrate the centering and scaling parameters (μ_N, σ_N) for $N = 500$ and $\alpha = 0$ by matching three quantiles between $F_N^{(L)}$ and F_2 . This yields $\mu_{500} \approx 1999.86$ and $\sigma_{500} \approx 19.85$, very close to the expected edge and $N^{1/3}$ scale. On $x \in [-6, 6]$ the scaled LUE CDF $F_{500}^{(L)}(\mu_{500} + \sigma_{500}x)$ and $F_2(x)$ then differ by at most about 2.6×10^{-3} , with typical errors near 10^{-3} in the central region.

8 Global limitations, Hamiltonian attempts, and future directions

The experiments above show that, when heavily constrained by Fredholm data, Painlevé σ –forms can be used to reconstruct finite- n gap probabilities with 10^{-3} – 10^{-5} accuracy across GUE, LUE, and JUE. At the same time they reveal several structural limitations of this approach and point towards more robust analytic tools.

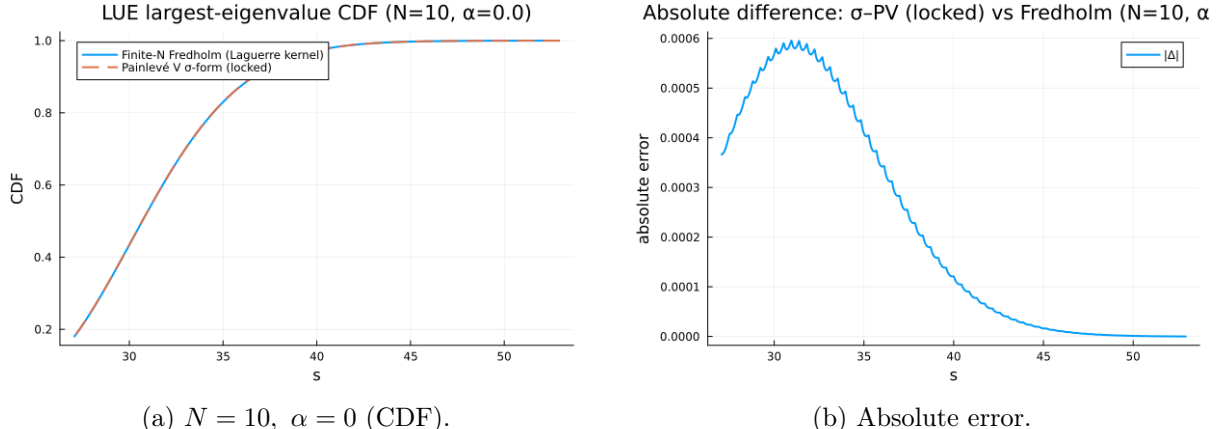


Figure 13: LUE: Fredholm vs. locked σ -PV (case 4).

Table 5: Maximum absolute error $\max_s |F_N^{(\text{Fred})}(s) - F_N^{(\sigma\text{-PV})}(s)|$ and run parameters (LUE).

N	α	$\max \Delta $	M (GL)	#anchors	s_{\min}	s_{\max}
100	5	1.54×10^{-4}	280	101	382.089	437.789
50	2	1.99×10^{-4}	260	91	181.876	226.085
20	0	2.87×10^{-4}	240	81	63.713	96.287
10	0	5.95×10^{-4}	220	61	27.073	52.927

8.1 Anchors, near interpolation, and sensitivity to perturbations

The core strategy of the paper is to view the Painlevé σ -equations as dynamical constraints between a relatively dense set of Fredholm anchors. At each anchor we estimate F , $\sigma = \frac{d}{ds} \log F$, and σ' from the Fredholm determinant, and between anchors we integrate the ODE with branch locking. This produces a smooth CDF that interpolates the Fredholm values and uses the ODE only to regularise the behaviour between anchors.

As a consequence, the method is extremely sensitive to the density and quality of anchors. If we halve the number of anchors while keeping the same ODE tolerances, the maximum error between the anchored Painlevé solution and the Fredholm CDF increases significantly, and in extreme cases the ODE may drift to a different branch between sparsely spaced anchors before being pulled back at the next anchor. In this sense the method behaves more like a specially constrained interpolation of Fredholm data than a free-standing ODE solver.

A related observation is that we cannot use this scheme to distinguish between the *exact* PIV σ -equation

$$(\sigma'')^2 = 4(s\sigma' - \sigma)^2 - 4(\sigma')^2(\sigma' + 2n)$$

and a slightly perturbed variant such as

$$(\sigma'')^2 = 4(s\sigma' - \sigma)^2 - 4(\sigma')^2(\sigma' + 2n + 0.01).$$

Numerically, the 0.01 perturbation in the coefficient of $(\sigma')^3$ only produces a difference of order 10^{-6} in F_n , while our overall error budget from quadrature, Fredholm truncation, and anchor extraction is of order 10^{-3} . In experiments where we deliberately replaced $2n$ by $2n + 0.01$ and repeated the anchored integration, the resulting CDFs remained within the observed error bands.

On the other hand, the ODE evolution between anchors *does* discriminate between genuinely different Painlevé-type equations. If we change the algebraic relation for σ'' to something

structurally different, such as

$$(\sigma'')^2 = 4(s\sigma' - \sigma)^2 - 4(\sigma' - n)(\sigma' - n - 1)\sigma'$$

or

$$(\sigma'')^2 = 4(s\sigma' - \sigma + n)^2 - 4(\sigma')^2(\sigma' + 2n + 1) + 3(\sigma')^4,$$

and keep the same anchor data, the resulting anchored CDF develops visible discrepancies of order 10^{-2} compared to the Fredholm curve. This shows that the ODE is not completely dominated by the anchoring; it does enforce the correct local dynamics and is able to reject radically different Painlevé models, even if it cannot reliably distinguish very small parameter shifts.

Readers interested in the detailed numerical experiments for P_{IV} are encouraged to inspect the GitHub repository

<https://github.com/hgu2699/Numerically-solve-Painleve-differential-equations>

and, in particular, the folder entitled *Painleve IV anchor method*, which contains the Julia scripts and plots used to compare different P_{IV} -type equations and study the effect of anchor spacing.

8.2 Hamiltonian formulation and movable poles

Since σ_n can be expressed as an affine function of the Okamoto Hamiltonian $H(s; q, p)$, one natural idea is to integrate the Hamiltonian system (11) directly for (q, p) , anchored by an asymptotic expansion at large s , and then reconstruct F_n via H . This Hamiltonian approach is emphasised in Forrester–Witte [2] and in the broader Painlevé literature.

We implemented such a scheme for $n = 20$ by computing high-order large- s asymptotics of (q, p) symbolically in Sage, feeding those expansions into Julia, and using a Hamiltonian IVP anchored at $s_0 = 6.4$ with (q, p) chosen to match both the asymptotics and the Fredholm values of H and H' at s_0 . The corresponding code and error logs can be found in the GitHub folder *Painleve IV Hamilton system asymptotic method*.

In practice the Hamiltonian IVP failed when integrating backwards from $s_0 = 6.4$ to $s = 5.0$: the adaptive solver repeatedly reduced the stepsize until it hit the machine epsilon threshold near $s \approx 5.65$, at which point it aborted with an error indicating that the estimated local truncation error could not be controlled. This behaviour is strongly suggestive of encountering a movable pole of the P_{IV} solution or of drifting onto a branch with a pole in the real direction. The failure occurred despite starting from carefully tuned asymptotic data and demonstrates how delicate the branch selection problem is in the Hamiltonian formulation when one treats it as a pure IVP without continual re-anchoring to Fredholm data.

While we did not attempt to stabilise the Hamiltonian IVP further (for example by moving the anchor deeper into the tail or by working in higher precision), the experiment confirms that the difficulties seen for the σ -form are not artefacts of the σ -representation alone but manifestations of the underlying movable-singularity structure of P_{IV} .

8.3 Other limitations and potential improvements

Several more practical limitations are shared across all ensembles:

1. **Fredholm conditioning.** For large n the Nyström matrices for the Hermite, Laguerre, and Jacobi kernels become ill conditioned near the edge, and many entries are at or below machine epsilon. This affects the eigenvalues of $I - A$ and limits the meaningful precision in $\log \det(I - A)$.

2. **Polynomial fitting of $\log F$.** Our estimates of σ and σ' at each anchor rely on local least-squares fits to $\log F(s)$. In regions where F is extremely close to 0 or 1 this becomes numerically fragile, since $\log F$ underflows or is dominated by roundoff. More stable alternatives include Savitzky–Golay filters or global spectral fits.
3. **ODE stiffness and branch locking.** The algebraic σ -forms are stiff near the edges and depend explicitly on n . Implicit or stiffly accurate Runge–Kutta methods would be better suited here than explicit schemes, especially for large n or for equations with strong nonlinearities.
4. **Quadrature design.** We used simple Gauss–Legendre rules on truncated intervals. For extreme tails or very large N one could gain robustness by using quadratures tailored to the underlying weights (Gauss–Hermite, Gauss–Laguerre, Gauss–Jacobi) or by employing double-exponential maps to capture endpoint singularities more accurately.

All of these are incremental improvements that would sharpen the numerics but not change the basic picture: without external constraints, Painlevé IV/VI IVPs are numerically unstable for the random-matrix branches of interest; with a dense enough set of Fredholm anchors, they become usable but behave more like constrained interpolants than independent solvers.

8.4 Riemann–Hilbert methods as a more intrinsic approach

The Riemann–Hilbert (RH) approach offers a conceptually different way of encoding Painlevé transients and random-matrix kernels that bypasses many of these IVP pathologies. In the RH framework, one formulates a matrix-valued boundary-value problem for a piecewise analytic function $Y(z)$ with prescribed jumps across contours in the complex plane and normalisation at infinity. Orthogonal polynomials, random-matrix kernels, and Painlevé functions all admit such characterisations, and asymptotics can be extracted via the Deift–Zhou nonlinear steepest descent method [4, 18].

For Painlevé equations specifically, the RH boundary data encode the monodromy of an associated linear system. The solution of the RH problem then *automatically* produces the Painlevé transcendent with the correct monodromy, and the Painlevé property (no movable branch points or essential singularities) follows from the analytic structure of the RH problem. This perspective is developed in depth in the monograph of Fokas, Its, Kapaev, and Novokshenov [18] and, for P_{IV} in particular, in the work of van der Put and Top [17, 34].

From the random-matrix side, RH problems for orthogonal polynomials with varying weights are the basis of the modern analysis of unitary ensembles [4] and of double-scaling and critical-edge phenomena [32, 33]. In this setting the Painlevé functions appear naturally as parametrices in local RH model problems near critical points, and the same RH problem simultaneously controls both the kernel and the associated Painlevé transcendent.

For our purposes, an RH-based numerical strategy for the finite- n GUE gap would look schematically as follows:

1. Set up the 2×2 RH problem for Hermite polynomials with the GUE weight, with n appearing as a parameter in the jump matrix.
2. Use a deformation of contours and small-norm arguments (in the sense of Deift–Zhou) to reduce the problem to a numerically stable one on a fixed contour, possibly with local parametrices near the soft edge.
3. Extract both the kernel entries and the Painlevé P_{IV} Hamiltonian or σ -function directly from the RH solution, using the known identifications between orthogonal polynomial RH problems and isomonodromic deformations.

The key point is that the RH problem encodes the *global* analytic and monodromy data that define the correct Painlevé branch. There is no need to guess initial conditions or to fight with movable poles via IVPs; instead, one solves a boundary-value problem whose solution is unique and analytic by construction. In particular, the RH representation should be robust under continuation into the bulk and should not suffer from the drift we control in the anchored ODE scheme by repeatedly resetting at Fredholm anchors.

There is a growing numerical literature on solving RH problems directly (see, for example, the work of Reeger and Fornberg [13, 14] in combination with RH packages), and it would be natural to bring these tools to bear on the random-matrix P_{IV} and P_{VI} branches studied here. This lies beyond the scope of the present paper but provides a promising direction in which branch selection, asymptotics, and numerical stability are all handled within a single integrable-structure framework.

Acknowledgments

The author wants to thank Professor Alan Edelman at MIT for guidance and supervision of this numerical analysis project. All computations were performed in Julia 1.9 using `OrdinaryDiffEq`, `FastGaussQuadrature`, and `LinearAlgebra`. The plots and Julia scripts used to generate the figures are available at

<https://github.com/hgu2699/Numerically-solve-Painleve-differential-equations>.

For the anchored P_{IV} scheme, see the folder *Painleve IV anchor method*; for the Hamiltonian IVP and asymptotic matching experiments, see *Painleve IV Hamilton system asymptotic method*.

References

- [1] C. A. Tracy and H. Widom. Level-spacing distributions and the Airy kernel. *Comm. Math. Phys.*, 159(1):151–174, 1994.
- [2] P. J. Forrester and N. S. Witte. Application of the τ -function theory of Painlevé equations to random matrices: PIV, PII and the GUE. *Comm. Math. Phys.*, 219(2):357–398, 2001.
- [3] M. Adler, T. Shiota, and P. van Moerbeke. Random matrices, vertex operators and the Virasoro algebra. *Phys. Lett. A*, 208(1-2):67–78, 1995.
- [4] P. Deift. *Orthogonal Polynomials and Random Matrices: A Riemann–Hilbert Approach*. Courant Lecture Notes, 1999.
- [5] F. Bornemann. On the numerical evaluation of Fredholm determinants. *Math. Comp.*, 79(270):871–915, 2010.
- [6] C. A. Tracy and H. Widom. Level-spacing distributions and the Bessel kernel. *Comm. Math. Phys.*, 161(2):289–309, 1994.
- [7] P. J. Forrester. *Log-Gases and Random Matrices*. Princeton University Press, 2010.
- [8] P. J. Forrester and N. S. Witte. Application of the τ -function theory of Painlevé equations to random matrices: PV, PIII, the LUE, JUE, and CUE. *Comm. Pure Appl. Math.*, 55(6):679–727, 2002.
- [9] P. J. Forrester and N. S. Witte. Application of the τ -function theory of Painlevé equations to random matrices: PVI, the JUE, CyUE, cJUE and scaled limits. *Nagoya Math. J.*, 174:29–114, 2004.
- [10] A. B. J. Kuijlaars and M. Vanlessen. Universality for eigenvalue correlations at the origin of the spectrum. *Comm. Math. Phys.*, 243(1):163–191, 2003.
- [11] I. M. Johnstone. Multivariate analysis and Jacobi ensembles: Largest eigenvalue, Tracy–Widom limits and rates of convergence. *Ann. Statist.*, 36(6):2638–2716, 2008.
- [12] B. Fornberg and J. A. C. Weideman. A numerical methodology for the Painlevé equations. *J. Comput. Phys.*, 230(15):5957–5973, 2011.
- [13] J. A. Reeger and B. Fornberg. Painlevé IV with both parameters zero: A numerical study. *Stud. Appl. Math.*, 130(2):108–133, 2013.
- [14] J. A. Reeger and B. Fornberg. Painlevé IV: A numerical study of the fundamental domain and beyond. *Physica D*, 280–281:1–13, 2014.
- [15] D. Dai and A. B. J. Kuijlaars. Painlevé IV asymptotics for orthogonal polynomials with respect to a modified Laguerre weight. *Stud. Appl. Math.*, 122(1):29–83, 2009.
- [16] M. Bertola, J.-M. Elias Rebelo, and T. Grava. Painlevé IV critical asymptotics for orthogonal polynomials in the complex plane. *SIGMA*, 14:091, 2018.
- [17] M. van der Put and J. Top. A Riemann–Hilbert approach to Painlevé IV. *J. Nonlinear Math. Phys.*, 20(sup1):164–176, 2013.
- [18] A. S. Fokas, A. R. Its, A. A. Kapaev, and V. Y. Novokshenov. *Painlevé Transcendents: The Riemann–Hilbert Approach*. Math. Surveys and Monographs, Vol. 128. AMS, 2006.
- [19] R. Conte. *The Painlevé Handbook*. Springer, 2014.

- [20] A. Deaño and N. J. Simm. On the probability of positive-definiteness in the gGUE via semi-classical Laguerre polynomials. *J. Approx. Theory*, 219:44–59, 2017.
- [21] A. Deaño and N. J. Simm. Characteristic polynomials of complex random matrices and Painlevé transcendent. *Int. Math. Res. Not.*, 2022(1):210–264, 2022.
- [22] M. Cao, Y. Chen, and J. Griffin. Continuous and discrete Painlevé equations arising from the gap probability distribution of the finite n GUE. *J. Stat. Phys.*, 157(2):363–375, 2014.
- [23] D. Dominici. Asymptotic analysis of the Hermite polynomials from their differential–difference equation. *J. Difference Equ. Appl.*, 13(12):1115–1128, 2007.
- [24] C. Charlier and A. Deaño. Asymptotics for Hankel determinants associated to a Hermite weight with a varying discontinuity. *SIGMA*, 14:018, 2018.
- [25] S. Lyu, Y. Chen, and E. G. Fan. Asymptotic gap probability distributions of the GUE and JUE. *Nucl. Phys. B*, 926:639–670, 2018.
- [26] E. Basor, Y. Chen, and L. Zhang. PDEs satisfied by extreme eigenvalues distributions of GUE and LUE. *Random Matrices Theory Appl.*, 1(1):1150003, 2012.
- [27] D. Dai. Asymptotics of orthogonal polynomials and the Painlevé transcendent. *SIGMA*, 12:057, 2016.
- [28] J. Schiff. A dynamical systems approach to the fourth Painlevé equation. *J. Phys. A*, 52(14):145201, 2019.
- [29] V. L. Vereshchagin. Global asymptotic formulae for the fourth Painlevé transcendent. *Sb. Math.*, 79(1):41–73, 1994.
- [30] E. A. Coddington and N. Levinson. *Theory of Ordinary Differential Equations*. McGraw–Hill, New York, 1955.
- [31] E. Hairer, S. P. Nørsett, and G. Wanner. *Solving Ordinary Differential Equations I: Nonstiff Problems*. Springer Series in Computational Mathematics, 2nd edition, 1993.
- [32] T. Claeys. Multi-critical unitary random matrix ensembles and the generalised Painlevé II equation. *Ann. of Math.*, 168(2):601–641, 2008.
- [33] P. Bleher and A. Its. Double scaling limit in the random matrix model: the Riemann–Hilbert approach. *Comm. Pure Appl. Math.*, 56(4):433–516, 2003.
- [34] M. van der Put and J. Top. A Riemann–Hilbert approach to Painlevé IV. *J. Math. Soc. Japan*, 65(2):491–512, 2013.